Computers and Geotechnics 166 (2024) 105972

Contents lists available at ScienceDirect

Computers and Geotechnics

journal homepage: www.elsevier.com/locate/compgeo

A 2D energy-conserving contact model for the combined finite-discrete element method (FDEM)

Weibing Cai [a], Ke Gao [a,b,*], Shugang Ai [a], Sheng Zhi [c]

[a] Department of Earth and Space Sciences, Southern University of Science and Technology, Shenzhen 518055, Guangdong, China
[b] Guangdong Provincial Key Laboratory of Geophysical High-resolution Imaging Technology, Southern University of Science and Technology, Shenzhen 518055, Guangdong, China
[c] Department of Risk Management, China Huarong International Holdings Limited, Hong Kong, China

ARTICLE INFO

Keywords:
Combined finite-discrete element method (FDEM)
Contact algorithm
Energy-conserving contact model
Contact force calculation
Arbitrarily shaped bodies

ABSTRACT

The combined finite-discrete element method (FDEM) has been widely used to simulate the progressive fracturing of brittle materials from continua to discontinua. However, due to the relatively simple definition of contact potential, the contact interaction algorithm utilized in the original FDEM is element size-dependent. As a result, a non-smooth and fluctuating contact force direction can occur when a contact point moves from one area of an element to another, and the contact interaction algorithm may fail to accurately evaluate the tangential contact force. To circumvent these limitations, we adopt an energy-conserving model developed recently to calculate the contact force in 2D FDEM, in which the magnitude and direction of contact force can be directly determined by geometrical features. A suite of numerical benchmarks is conducted to validate the effectiveness and robustness of the proposed method for contact interaction processing between discrete bodies, and the advantages of the proposed method are also demonstrated. As an application, two typical examples are performed to systematically explore the potential of the proposed approach for evaluating the stability of rock mass and rock slope. The proposed contact model may help enhance the applicability and accuracy of FDEM for rock fracturing simulation.

1. Introduction

The combined finite-discrete element method (FDEM) (Munjiza, 1992), with its capability of bridging the continuum analysis using finite element method (FEM) and the discontinuum simulations using discrete element method (DEM), provides an effective solution to simulate the fracturing behavior of brittle materials such as rocks (Chen et al., 2020; Euser et al., 2019; Wu et al., 2021). In FDEM, the modeling domain is first discretized into a series of finite elements, and zero-thickness cohesive elements are inserted into the common boundaries between adjacent finite elements prior to simulation. The finite elements can capture the deformation and stress evolution in the solid domain, and cohesive elements can simulate the inter-element crack initiation, propagation and coalescence (Munjiza, 2004). To date, FDEM has been extensively applied in various scientific and engineering problems, such as blasting (Han et al., 2020b; Wang et al., 2021; Yang et al., 2020), discrete fracture networks (Lei and Gao, 2018; Lei et al., 2021), tunnel excavation (Han et al., 2020a), acoustic emission monitoring (Lisjak et al., 2013; Zhao et al., 2014; Zhao et al., 2015) and multi-physics/field coupling (Xiang et al., 2022; Yan et al., 2018; Yan et al., 2022).

During the progressive fracturing progress in rock masses, accurately estimating the contact interaction between fracture surfaces is crucial to capturing the post-failure behaviors. To effectively handle complex contact or dynamic impact problems, a potential-based penalty function method was initially proposed by Munjiza (2004). In the original FDEM, taking the 2D model for example, each triangle element in contact is divided into three sub-triangles according to the location of the contact, and the contact potential can be defined as the minimum shape functions at the target point in the corresponding sub-triangle (Lei et al., 2020). Based on Green's formula, the calculation of the normal contact force of the overlap area is simplified as an integral of the potential on the boundary of the contactor element, and the direction of normal contact force can also be directly obtained by the outward normal direction of the boundary (Munjiza, 2004). However, due to the relatively simple definition of contact potential in the original FDEM, the calculated magnitude and direction of contact forces are sensitive to element

* Corresponding author at: Department of Earth and Space Sciences, Southern University of Science and Technology, Shenzhen 518055, Guangdong, China.
E-mail address: gaok@sustech.edu.cn (K. Gao).

https://doi.org/10.1016/j.compgeo.2023.105972
Received 6 August 2023; Received in revised form 25 October 2023; Accepted 21 November 2023

size (see Section 3.3), thereby may occasionally result in spurious contact force fluctuation (Lei et al., 2020; Liu et al., 2020; Yan and Zheng, 2017; Zhao et al., 2018b).

To alleviate these issues, by combining the characteristic length of mesh and the point-to-edge distance, Yan and Zheng (2017) redefined the contact potential, which avoids the dependence of element size on contact force calculation in particular cases. With a clear physical meaning, a novel distance potential function using a normalized penetration distance between contact couples was also proposed to calculate normal contact forces (Zhao et al., 2018a,2018b). However, those methods can obtain accurate contact force only when each discrete body is represented by a single finite element (Lei et al., 2020; Liu et al., 2022b). Whereas for larger overlap areas between contact objects, the normal contact force may decrease with the increase of contact areas, which no doubt violates the physics that contact force should be a monotone increasing function of contact areas. Additionally, those methods may also encounter non-smooth and fluctuating contact force when the contact point (where contact force is applied and the total moment is zero) moves from one sub-triangle to another. Recently, a smooth potential field based on the global geometrical information of discrete bodies has been introduced to solve the numerical non-smoothness of contact force (Lei et al., 2020). Instead of using the traditional "triangle-to-triangle" contact regime, this method adopts a "triangle-to-node" approach to calculate contact forces by discretizing the edges of the target finite element with Gaussian integration points (target points), and is thus suitable for both concave and convex bodies of complex shapes. However, the frequent update of the contact potential field induced by the generation of fracture and fragment inevitably reduces the computational efficiency (Liu et al., 2022b). Therefore, it is necessary to explore robust and efficient contact algorithms within the current framework of FDEM.

Generally, an appropriate contact model for contact interaction should possess clear geometric features and a simple physical law (Feng 2021b). The geometric features are associated with contact areas, contact force direction, and contact point location; the physical aspect requires appropriate selection of suitable contact interaction law to obtain the magnitude of contact force and to capture the physical behaviors of contact in terms of the contact geometric features. Taking the rigid-particle-based DEM originally proposed by Cundall and Strack (1979) for example, the contact geometric features of disk/sphere can be straightforwardly described, and the magnitude of the normal contact force is defined as a linear or nonlinear function of the overlap area. That is, the contact geometric features are independent of the physical law. The DEM has broad applications in brittle rock-related simulations due to its simplicity of element type and high computational efficiency in contact detection and contact interaction (Gu et al., 2020). However, it is well known that the circular/spherical bodies lack highly interlocked grain structures, which fails to simulate rocks with low strength ratio (i.e., the ratio between tensile strength and uniaxial compressive strength) and high macro friction coefficient (Potyondy and Cundall, 2004). For irregular discrete bodies with arbitrary shapes, the contact geometric features are no longer uniquely defined, and the body shape can affect the overall physical behavior of the discrete system. For example, the vertex-to-vertex contact situation may encounter discontinuity and non-smoothness of contact force at the corner of polygon bodies, which inevitably leads to local stress fluctuation. The same problem has been reported in commercial and research codes such as UDEC (Universal Distinct Element Code) (Board, 1989) and DDA (Discontinuous Deformation Analysis) (Shi and Goodman, 1985).

Fortunately, a unified theoretical framework has been gradually established for developing energy-conserving contact models for arbitrarily shaped discrete bodies (Feng 2021b, 2021c; Feng et al., 2012). This type of contact model not only has the advantages of energy conservation for elastic impacts, but also can automatically obtain the contact normal direction, contact point and force magnitude without explicitly defining the contact potential. Thus, the contact geometric features and physical laws in such models are closely related, and different combinations of geometric features as variables for the contact energy function can generate various energy-conserving contact models. Compared to the potential-based penalty function method commonly utilized in FDEM, the energy-conserving contact models can effectively circumvent the dependence of element size on contact force calculation, and avoid the unstable contact force (as will be proved in Sections 3.3 and 3.4) (Lei et al., 2020). Notably, without the need to define the contact potential of Gaussian integration points, the energy-conserving contact models can slightly reduce the computation costs by directly calculating the gradient of geometric features to coordinate vector (as will be illustrated in Section 3.6) (Liu et al., 2022b). This type of contact model has been successfully applied in DEM for simulating the mechanical behaviors of granular media with arbitrarily shaped rigid particles (Gao and Feng, 2019; Lai et al., 2022; Liu et al., 2022a). There is also evidence that an energy-conserving contact model has been implemented in 3D FDEM by Liu et al., (2022b); however, the contact point in this FDEM implementation is approximately taken as the mass center of overlap volumes. Such a definition of mass center can only guarantee correct contact force calculation for small overlap volumes.

To sum up, an appropriate definition of contact potential is crucial for accurate contact force calculation; however, in the original FDEM, such a definition is challenging (Lei et al., 2020; Yan and Zheng, 2017; Zhao et al., 2018b). Although much effort has been made to circumvent this problem, establishing a contact potential field considering solid fracturing is difficult. The energy-conserving contact models proposed by Feng (2021a) can automatically obtain the contact direction, contact point and force magnitude without explicitly defining the contact potential, which simplifies the contact force calculation process. In this work, based on our 2D in-house FDEM code – Pamuco (**Par**allel • **mu**ltiphysics • **co**upling), we adapt the energy-conserving contact model developed by Feng (2021a) to better accommodate the contact interaction process in FDEM, and simulate the collisions between arbitrarily shaped deformable bodies. Compared to the work by Feng (2021a), we have also made the following improvements in the present paper: (i) except for the normal contact force computation, the calculation of tangential contact force and its detailed realization procedure in FDEM is also systematically introduced; (ii) more details about the determination of geometrical features in the framework of FDEM, such as contact area, contact point and normal contact direction, are provided; (iii) the deformation and stress of discrete bodies in contact can be well captured.

The paper is organized as follows. In Section 2, the explicit solution approach based on the energy-conserving contact model is briefly introduced in the framework of FDEM. Additionally, we systematically illustrate how to determine the contact overlap area and calculate the contact force (normal and tangential) using the energy-conserving contact model for triangle finite elements. In Section 3, a series of benchmark cases are performed to validate the accuracy and robustness of the proposed method for contact force calculation between discrete bodies. The advantages of the proposed method are also demonstrated in comparison to the original contact algorithm proposed by Munjiza (2004). Following this, two typical application cases are presented in Section 4 to demonstrate the potential of the proposed method in evaluating the stability of rock mass and rock slope. Conclusions are drawn in Section 5.

2. Theories

In this section, we first introduce the governing equation, explicit solution scheme, and the constitutive laws of finite elements in FDEM. Then, the energy-conserving contact theory for normal and tangential contact force calculation is systematically illustrated.

2.1. Governing equation

In a 2D FDEM model, the solid matrix is discretized into an assembly of triangle finite elements, and explicit time integration schemes are adopted to solve the motion equations. Generally, the governing equation in FDEM can be expressed as (Munjiza, 2004)

$$\mathbf{M}\ddot{\mathbf{u}} + \mathbf{C}\mathbf{u} = \mathbf{f} \tag{1}$$

where $\mathbf{M}$ is the mass matrix, $\mathbf{C}$ is the damping matrix, $\mathbf{u}$ is the node displacement vector, and $\mathbf{f}$ represents the total force vector. The damping matrix is introduced to consume kinetic energy for quasi-static cases, i.e., the so-called dynamic relaxation, which can be calculated by

$$\mathbf{C} = \eta\mathbf{I} \tag{2}$$

where η and $\mathbf{I}$ are the damping coefficient and identity matrices of finite elements, respectively. The FDEM uses the central difference scheme to update the displacement and velocity of nodes at each simulation timestep. Then, the velocity of each node can be obtained by (Munjiza, 2004)

$$\dot{\mathbf{u}}(t+\Delta t) = \dot{\mathbf{u}}(t) + \ddot{\mathbf{u}}(t)\cdot\Delta t \tag{3}$$

where Δt is the timestep, and t and $t + \Delta t$ denote the previous and current time instants, respectively. The displacement vector $\mathbf{u}(t+\Delta t)$ of the node can be updated using (Munjiza, 2004)

$$\mathbf{u}(t+\Delta t) = \mathbf{u}(t) + \dot{\mathbf{u}}(t+\Delta t)\cdot\Delta t \tag{4}$$

In FDEM, the ultimate timestep Δt is the smaller value of the required stability timestep between FEM and DEM (Guo et al., 2015), i.e.,

$$\Delta t = \min\{\Delta t_{FEM}, \Delta t_{DEM}\} \tag{5}$$

Here

$$\Delta t_{FEM} \sim \frac{h}{10}\sqrt{\frac{\rho}{E}} \tag{6}$$

and

$$\Delta t_{DEM} \sim \frac{\pi}{5}\sqrt{\frac{m}{P_n}} \tag{7}$$

where Δt_{FEM} and Δt_{DEM} are the required timestep of FEM and DEM, respectively, ρ is the density, E is the Young's modulus, h is the minimum length of triangle elements, m is the minimum mass of one single triangle element, and P_n is the contact stiffness between the contact couples.

2.2. Constitutive equation

Unlike the collision of rigid bodies in traditional DEM, we can obtain the detailed stress and deformation distribution of bodies during the contact process in FDEM. The mechanical behavior of constant strain finite elements can be expressed by (Munjiza, 2004)

$$\boldsymbol{\sigma}_{ij} = \frac{\lambda}{2}\left(J - \frac{1}{J}\right)\boldsymbol{\delta}_{ij} + \frac{\mu}{J}\left(\mathbf{B}_{ij} - \boldsymbol{\delta}_{ij}\right) + \eta\mathbf{D}_{ij} \quad (i,j = 1, 2) \tag{8}$$

Here

$$\mathbf{B}_{ij} = \mathbf{u}_{i,j} + \mathbf{u}_{j,i} \tag{9}$$

and

$$\mathbf{D}_{ij} = \frac{1}{2}\left(\mathbf{v}_{i,j} + \mathbf{v}_{j,i}\right) \tag{10}$$

where $\boldsymbol{\sigma}_{ij}$ represents the Cauchy stress tensor, λ and μ are the Lame constants, $\mathbf{u}_{i,j}$ and $\mathbf{u}_{j,i}$ are both the deformation gradient tensor, $\mathbf{v}_{i,j}$ and $\mathbf{v}_{j,i}$ are both the velocity gradient tensor, $\mathbf{B}_{ij}$ denotes the left Cauchy-Green deformation tensor, $\mathbf{D}_{ij}$ is the rate of deformation tensor, J is the determinant of deformation gradient, η is the viscous damping coefficient, and $\boldsymbol{\delta}_{ij}$ is the Kronecker delta.

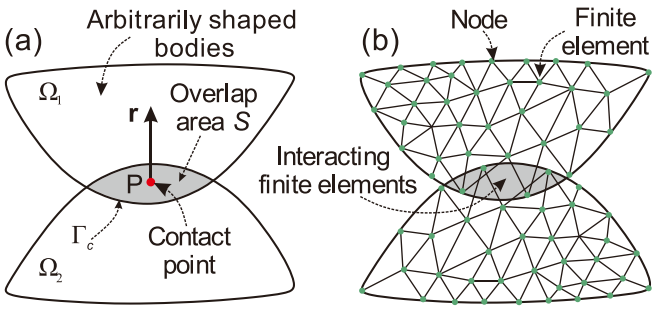

Fig. 1. (a) Two arbitrarily shaped bodies Ω_1 and Ω_2 in contact and their contact region. (b) Discretization of the two discrete body domains. The contact point is denoted as point P (marked by a red dot), whose coordinate vector is represented by $\mathbf{x}_P$; the contact areas and boundaries are presented by S and Γ_c, respectively; and $\mathbf{r}$ is the normal direction of contact force. (For interpretation of the references to colour in this figure legend, the reader is referred to the web version of this article.)

The boundary conditions are (Ju et al., 2016)

$$u_i = \bar{u}_i, \quad \boldsymbol{\sigma}_{ij}\mathbf{n}_j = \mathbf{T}_i \tag{11}$$

and the initial conditions are (Ju et al., 2016)

$$u_i(\mathbf{x}, t=0) = \bar{u}_i(\mathbf{x}), \quad \dot{u}_i(\mathbf{x}, t=0) = \bar{\dot{u}}_i(\mathbf{x}) \tag{12}$$

where $\mathbf{n}_j$ is the outward unit normal vector to the external surface, $\mathbf{T}_i$ is the externally applied traction force, u_i is the component of displacement vector $\mathbf{u}$, and $\mathbf{x}$ denotes the coordinate vector.

2.3. Contact model

The contact algorithm for processing the interaction between neighboring finite elements in FDEM involves contact detection and contact interaction. The contact detection of finite elements in touch is conducted to determine contact couples. The efficient NBS (non-binary search) algorithm is commonly used in FDEM for contact detection, which yields a theoretical CPU time proportional to the total number of finite elements (Munjiza and Andrews, 1998). After obtaining the contact couple lists, the contact interaction algorithm will be invoked to calculate the contact forces.

Here, the normal contact force is calculated by implementing the energy-conserving contact model developed earlier for arbitrarily shaped bodies (Feng 2021b, 2021c; Feng et al., 2012). Taking the two arbitrarily shaped 2D bodies Ω_1 and Ω_2 with overlap for example (Fig. 1a), the overlap or contact area S is the intersection of the two bodies, which generally determines the geometric aspect of the contact between the two bodies concerned, i.e.,

$$S \equiv \Omega_1 \cap \Omega_2 \neq \varnothing \tag{13}$$

where $\Gamma_c \equiv \partial S$ is the boundary of the overlap area S. Based on any reference point $(\mathbf{x}, \theta)$, we can define the corresponding contact force $\mathbf{F}_n$ and contact moment $\mathbf{M}_\theta$ acting at the reference point. Note that $\mathbf{x}$ is the coordinate vector and θ denotes the rotation of bodies with respect to the reference point. In 2D space, we can define a scalar potential function $\varphi(S)$ to describe the contact state, which has a sound physical explanation that the contact force and contact moment at the state will reduce the contact energy most effectively or at the largest rate, i.e.,

$$\mathbf{F}_n = -\nabla_{\mathbf{x}}\varphi(S) = -\frac{d\varphi(S)}{dS}\frac{\partial S}{\partial \mathbf{x}} = -\varphi'(S)\nabla_{\mathbf{x}}S = F_n\mathbf{r} \tag{14}$$

and

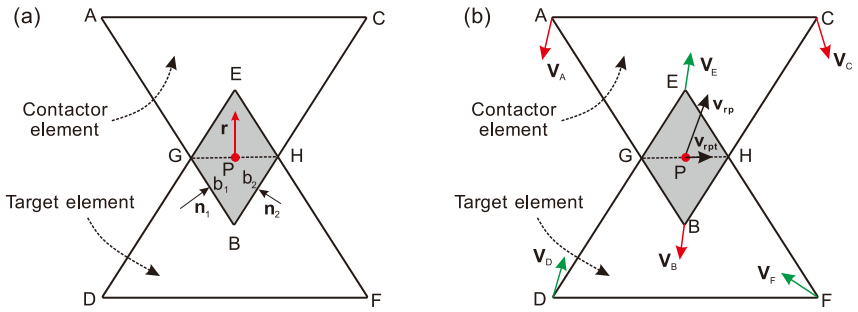

Fig. 2. (a) Two triangle elements in contact. (b) The velocities of nodes and contact point. The contact point is denoted as point P, and is marked by a red dot. (For interpretation of the references to colour in this figure legend, the reader is referred to the web version of this article.)

$$\mathbf{M}_\theta = -\nabla_\theta \varphi(S) = -\frac{d\varphi(S)}{dS}\frac{\partial S}{\partial \theta} = -\varphi^{'}(S)\nabla_\theta S \tag{15}$$

Here, ∇ denotes the gradient operator, F_n is the magnitude of normal contact force $\mathbf{F}_n$ between discrete bodies, and $\mathbf{r}$ is the direction of normal contact force. As pointed out in the previous works (Feng 2021b, 2021c; Feng et al., 2012), selecting a reference point in a solid body is arbitrary, which no doubt causes the non-determinacy of the calculated tangential contact force. Then we denote a contact point P, whose coordinate vector is represented by $\mathbf{x}_P$, to conveniently apply contact force on discrete bodies. The total contact moment is zero, i.e.,

$$(\mathbf{x}_P - \mathbf{x}) \times \mathbf{F}_n - \mathbf{M}_\theta = 0 \tag{16}$$

where

$$\mathbf{x}_P = \mathbf{x} + \frac{\mathbf{r} \times \mathbf{M}_\theta}{\|\mathbf{F}_n\|} + \lambda \mathbf{r} \tag{17}$$

$$\mathbf{r} = \mathbf{x}_P - \mathbf{x} \tag{18}$$

and λ is a free parameter and defines a fixed line (contact line) along the normal contact direction. Theoretically, any point on the contact line will result in the same normal motion of the bodies.

In FDEM, each of the two discrete bodies (e.g., Ω_1 and Ω_2) in touch is discretized into a series of triangle finite elements (see Fig. 1b). The contact between the two bodies can be simplified into contact between a series of triangle elements along the boundary Γ_c. These boundary elements can be further grouped into contact couples based on their relative positions, denoted as target and contactor elements. Due to the simple geometry of triangle elements, we can further simplify the calculation form of contact force defined by Eq. (14). Importantly, we can directly determine the coordinate vector of the contact point P for 2D triangle elements. For the contact couple (e.g., contactor element ΔABC and target element ΔDEF) shown in Fig. 2, we can obtain the following:

$$\nabla_{\mathbf{x}} S = \sum_{i=1}^{k} b_i \mathbf{n}_i \tag{19}$$

$$F_n = \varphi^{'}(S)\|\nabla_{\mathbf{x}} S\| \tag{20}$$

$$\mathbf{r} = -\frac{\nabla_{\mathbf{x}} S}{\|\nabla_{\mathbf{x}} S\|} \tag{21}$$

where k is the number of contact edges in the overlap area, b_i is the length of the ith contact edge, and $\mathbf{n}_i$ is the outward unit normal vector of the ith contact edge. Herein, we take the potential function as

$$\varphi(S) = \frac{S^2}{2S_d} P_n \tag{22}$$

where,

$$S_d = \frac{S_c + S_t}{2} \tag{23}$$

P_n is the normal penalty parameter, and S_c and S_t are the areas of contact couples. After determining all the intersecting points of contact couples, the corresponding contact directions and the overlap area can be easily obtained. Taking the intersecting point G between edges AB and DE shown in Fig. 2a for example, the distances between points D ($d_{\text{D-AB}}$) and E ($d_{\text{E-AB}}$) with respect to edge AB can be respectively obtained by

$$\begin{cases} d_{\text{D - AB}} = \dfrac{\overrightarrow{\mathbf{AB}} \times \overrightarrow{\mathbf{AD}}}{\left\|\overrightarrow{\mathbf{AB}}\right\|} \\ d_{\text{E - AB}} = \dfrac{\overrightarrow{\mathbf{AB}} \times \overrightarrow{\mathbf{AE}}}{\left\|\overrightarrow{\mathbf{AB}}\right\|} \end{cases} \tag{24}$$

Then the coordinate vector $\mathbf{x}_G$ of the intersection point G is determined by

$$\mathbf{x}_G = \left|\frac{d_{\text{D - AB}}}{d_{\text{D - AB}} - d_{\text{E - AB}}}\right| \mathbf{x}_E + \left(1 - \left|\frac{d_{\text{D - AB}}}{d_{\text{D - AB}} - d_{\text{E - AB}}}\right|\right) \mathbf{x}_D \tag{25}$$

where $\mathbf{x}_D$ and $\mathbf{x}_E$ are the coordinate vectors of points D and E, respectively. Other intersection points can be obtained similarly. As shown in Fig. 2a, the contact point P is the middle point of line GH, which has a clear geometric interpretation. More theoretical derivation about the determination of contact points is available in previous literature (Feng et al., 2012; Feng and Owen, 2004).

It is worth noting that the effect of tangential contact force is not considered in the energy-conserving contact model developed by Feng (2021a). To address this problem, we borrow the strategy from the original FDEM contact model, in which the tangential contact force is calculated based on the relative slipping displacement between contact couples upon using Coulomb's friction law. The relative velocity $\mathbf{V}_{\text{rp}}$ at contact point P is given by

$$\mathbf{V}_{\text{rp}} = \mathbf{V}_{\text{con}} - \mathbf{V}_{\text{tar}} \tag{26}$$

where $\mathbf{V}_{\text{con}}$ and $\mathbf{V}_{\text{tar}}$ are the velocities (see Fig. 2b) of the contactor and target element at contact point P, respectively, which can be calculated by

$$\mathbf{V}_{\text{con}} = N_{\text{A}}\mathbf{V}_{\text{A}} + N_{\text{B}}\mathbf{V}_{\text{B}} + N_{\text{C}}\mathbf{V}_{\text{C}} \tag{27}$$

and

$$\mathbf{V}_{\text{tar}} = N_{\text{D}}\mathbf{V}_{\text{D}} + N_{\text{E}}\mathbf{V}_{\text{F}} + N_{\text{F}}\mathbf{V}_{\text{F}} \tag{28}$$

Here, $\mathbf{V}_{\text{A}}$, $\mathbf{V}_{\text{B}}$, $\mathbf{V}_{\text{C}}$, $\mathbf{V}_{\text{D}}$, $\mathbf{V}_{\text{E}}$ and $\mathbf{V}_{\text{F}}$ are the nodal velocities (see Fig. 2b), and N_{A}, N_{B}, N_{C}, N_{D}, N_{E} and N_{F} are the shape functions satisfying $N_{\text{A}} + N_{\text{B}} + N_{\text{C}} = 1$ and $N_{\text{D}} + N_{\text{E}} + N_{\text{F}} = 1$. More details about the shape functions are available in previous literature (Munjiza, 2004; Munjiza et al., 2011). Then the tangential relative displacement

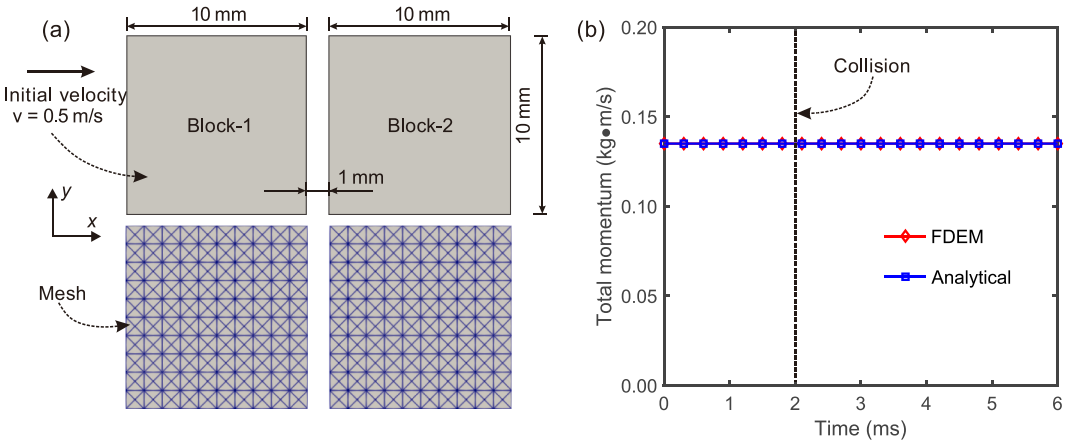

Fig. 3. (a) Initial configuration and mesh of the collision squares with identical geometry. (b) The total momentum of the two blocks in terms of analytical solution and FDEM simulation. The instant of collision between the two blocks is marked by a dashed line.

increment (Δu) within one timestep (Δt) is given by

$$\Delta u = V_{\text{rpt}} \Delta t \tag{29}$$

where V_{rpt} is the projection of $\mathbf{V}_{\text{rp}}$ on line GH. The contact tangential force can be updated incrementally by

$$\mathbf{F}_s = \mathbf{F}_s^{t-\Delta t} - P_s \Delta u \tag{30}$$

where $\mathbf{F}_s$ and $\mathbf{F}_s^{t-\Delta t}$ are tangential contact force at current and previous timesteps, respectively, and P_s is the tangential penalty parameter. If $|\mathbf{F}_s| \geq |\mathbf{F}_n|\mu$, then the tangential contact force can be calculated based on Coulomb's friction law, i.e.,

$$\mathbf{F}_s = \frac{\mathbf{F}_s}{|\mathbf{F}_s|} |\mathbf{F}_n| \mu \tag{31}$$

where $\mathbf{F}_n$ is the normal contact force at the contact point, and μ is the friction coefficient between contact couples. Finally, the total contact force $\mathbf{F}_{\text{total}}$ due to the penetration and friction acting on the contact point can be obtained by

$$\mathbf{F}_{\text{total}} = \mathbf{F}_n + \mathbf{F}_s \tag{32}$$

After this, the contact force will be resolved to the three nodes of the associated triangle elements. Combining with the Cauchy stress of triangle elements in the previous timestep, the nodal displacement and velocity in the current timestep can be updated according to Eq. (8), in order to prepare for the computation in the next timestep.

It is worth noting that the contact penalties (P_n and P_s) are numerical parameters defined as the ratio between contact force and contact area. Theoretically, the contact penalty should be infinity to avoid overlap between contact couples. In practice, too large a contact penalty will lead to a small timestep and thus increase the computational cost; however, too small a contact penalty may produce a significant overlap between contact couples. According to the previous works (Deng et al., 2021a; Deng et al., 2021b; Tatone and Grasselli, 2015), the contact penalty set as 1–100 times Young's modulus could achieve the balance between computational efficiency and accuracy.

3. Validation and comparison

In this section, several numerical tests, such as momentum conservation and frictional sliding tests, are first conducted to validate the accuracy of the proposed contact model in the current FDEM. Then, we show the robustness of the proposed approach for contact force calculation by comparing the results to the contact algorithm employed in the original FDEM (i.e., Munjiza's method). Although much effort has been made to improve the contact interaction in the original FDEM (Yan and Zheng, 2017; Zhao et al., 2018a,2018b), some deficiencies illustrated in Section 3.3–3.6 still exist in those contact models. Therefore, we only compare the results to the contact algorithm between our proposed method and Munjiza's method in this section due to the extensive application of the latter.

3.1. Momentum conservation

Block collision tests are first conducted to validate the correctness of the proposed contact model in terms of momentum conservation. As shown in Fig. 3a, the model consists of two identical square and frictionless blocks (Block-1 and Block-2) with an edge length of 10 mm. The parameters used for the two blocks are as follows: Young's modulus E = 30.0 GPa, Poisson's ratio $\nu = 0.25$, bulk density $\rho = 2700$ kg/m^3, contact penalty $P_n = P_s = 90$ GPa, and timestep $\Delta t = 3.0 \times 10^{-8}$ s. Contact friction is not considered here, and the viscous damping coefficient of finite elements is $\eta = 9.0 \times 10^3$ kg/m·s. The model consists of 800 triangle finite elements with an average size of 1 mm. Gravity is ignored, and the total simulation time is 6×10^{-3} s. Block-1 is stimulated with an initial

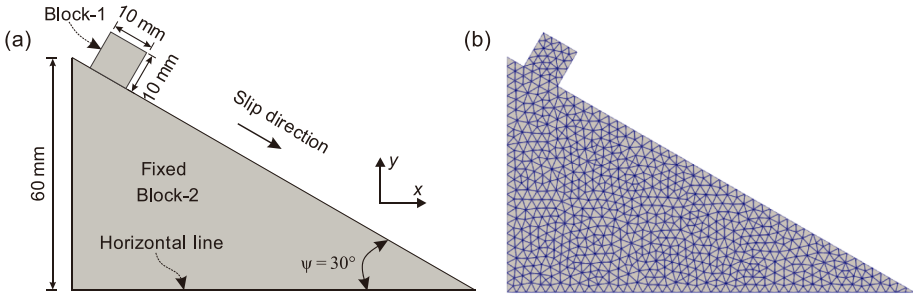

Fig. 4. (a) Initial configuration of the frictional experiment. (b) Mesh.

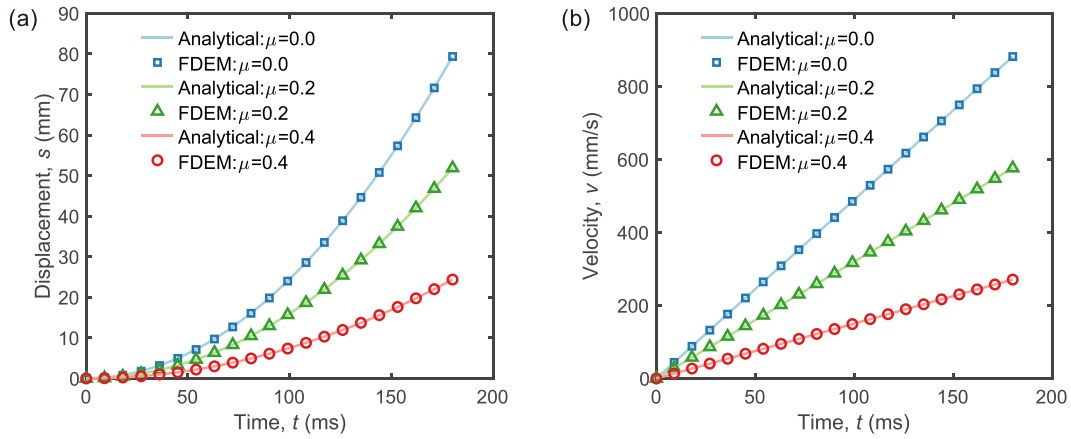

Fig. 5. (a) Displacement and (b) velocity of Block-1 along the inclined surface of Block-2 for the three friction coefficients between Block-1 and Block-2 (μ = 0, 0.2, 0.4).

horizontal velocity (along x axis) of 0.5 m/s toward Block-2. Note that the mass center velocities of the two blocks are monitored for calculating their momentums. The numerical results of the total momentum of Block-1 and Block-2 versus time are shown in Fig. 3b. The maximum difference between the FDEM simulated result and the analytical solution is ~ 3.7×10^{-10} kg•m/s, demonstrating the excellent accuracy of our implemented contact model in terms of momentum conservation.

3.2. Frictional experiment

The classic case of a sliding block on an inclined surface, as shown in Fig. 4a, is used to verify the accuracy of the proposed approach for contact force calculation. The model consists of one square block (Block-1) at the top and a triangle block (Block-2) at the bottom. The edge length of Block-1 is 10 mm. The lateral length of Block-2 is 60 mm, and the angle of the inclined surface is $\psi = 30^\circ$ with respect to the horizontal line. The parameters used for the model are as follows: Young's modulus E = 30.0 GPa, Poisson's ratio ν = 0.2, bulk density ρ = 2700 kg/m^3, contact penalty $P_n = P_s$ = 300 GPa, finite element viscous damping coefficient $\eta = 1.8 \times 10^4$ kg/m·s, and timestep $\Delta t = 6.0 \times 10^{-8}$ s. Block-2 is completely fixed. The model consists of 1352 triangle elements with an average size of 2.5 mm (see Fig. 4b), and the total simulation time is 0.18 s. If the selected equivalent friction angle between Block-1 and Block-2 is smaller than the inclined angle (i.e., 30°), Block-1 (with a zero initial velocity) will slide along the inclined surface of Block-2 under gravity. The analytical solution for the displacement s and velocity v of Block-1 along the inclined surface of Block-2 at time t are given by

$$s = \frac{1}{2} g(\sin\psi - \mu\cos\psi)t^2 \tag{33}$$

and

$$v = g(\sin\psi - \mu\cos\psi)t \tag{34}$$

respectively, where g is the gravitational acceleration (g = -9.8 m/s^2), and μ denotes the friction coefficient between Block-1 and Block-2. In addition, the analytical solutions for the normal and tangential contact force (F_n and F_s) between Block-1 and Block-2 are respectively

$$F_n = mg\cos\psi \tag{35}$$

and

$$F_s = \begin{cases} mg\sin\psi & \mu \geq \tan\psi \\ \mu F_n & \mu < \tan\psi \end{cases} \tag{36}$$

where m denotes the mass of Block-1.

The evolutions of displacement and velocity of Block-1 along the inclined surface of Block-2 for three friction coefficients between Block-1 and Block-2, i.e., μ = 0, 0.2, 0.4, are shown in Fig. 5. Note that these three selected friction coefficients can guarantee the slip of Block-1 along the inclined surface of Block-2. It can be seen that the displacement and velocity obtained from the FDEM simulation are in good agreement with the analytical solution (Eqs. (33) & (34)), which validates the accuracy of the proposed approach for block sliding test. In addition, to further test the proposed approach for capturing the contact

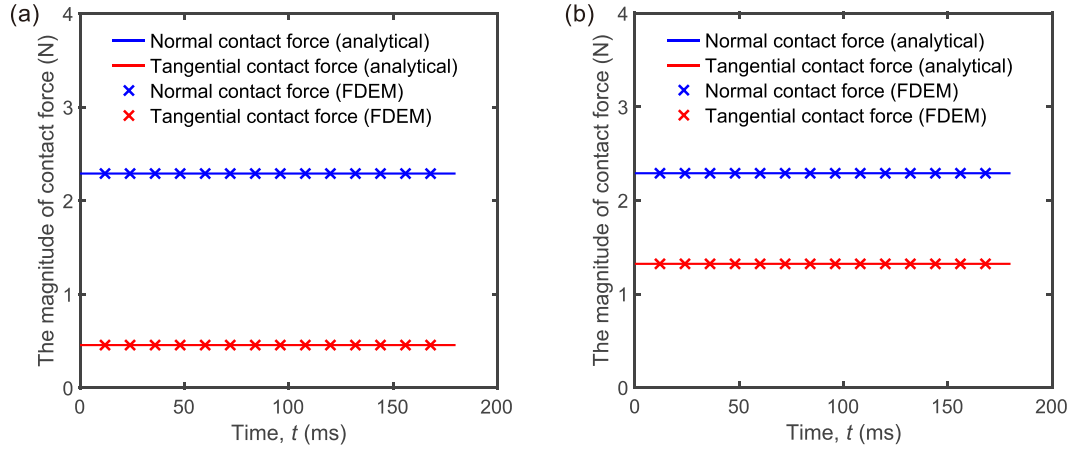

Fig. 6. Numerical and analytical results in terms of contact force magnitude between Block-1 and Block-2 for the two friction coefficients. (a) μ = 0.2. (b) μ = 0.8.

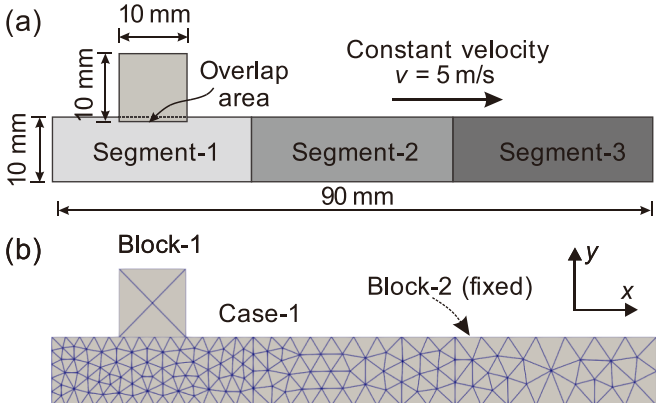

Fig. 7. (a) Model geometry and loading conditions. (b) Mesh for Case-1. The large rectangle block (Block-2) is evenly divided into three segments with different prescribed average element sizes.

Table 1
Different combinations of prescribed average element sizes for the three segments in Block-2.

Combination	Segment-1 (mm)	Segment-2 (mm)	Segment-3 (mm)
Case-1	2	3	5
Case-2	2	5	3
Case-3	3	2	5
Case-4	3	5	2
Case-5	5	2	3
Case-6	5	3	2

force magnitude, we select two friction coefficients, i.e., the previous $\mu = 0.2$ and a new $\mu = 0.8$, to create two scenarios in which Block-1 can slide and remain still on Block-2, respectively. As shown in Fig. 6, the normal and tangential contact force between Block-1 and Block-2 obtained from the FDEM simulation are consistent with the analytical solution (Eqs. (35) & (36)), which validates the accuracy of the proposed approach for contact force calculation.

3.3. Sensitivity of mesh size

As mentioned in previous FDEM works (Yan and Zheng, 2017; Zhao et al., 2018a,2018b), the definition of contact potential in the original FDEM (referred to as Munjiza's approach hereafter) is sensitive to element size. Here, we perform a series of contact tests to compare the normal contact forces calculated using Munjiza's and the proposed approach under the same overlap areas. As shown in Fig. 7a, the model contains one small square block (Block–1) and a large rectangle block (Block-2), where the edge length of Block-1 is 10 mm, and Block-2 has dimensions of 90 mm × 10 mm (width × height). Block-2 is divided into three equal-length segments (Segment-1, Segment-2 and Segment-3 from left to right) with different prescribed average element sizes for meshing. Six combinations of prescribed average element sizes for the three segments in Block–2 are tabulated in Table 1, which are successively numbered as Case-i ($i = 1, 2, \ldots, 6$), with the purpose of generating different scenarios to test the element size dependency of the two approaches. The unstructured Delaunay triangulation mesh scheme is used in the current analysis. For the model shown in Fig. 7a, since we use different prescribed mesh sizes for the three segments, there will be a smooth transition near the boundaries between adjacent segments in terms of yielded element size. This also indicates that for two segments in different cases using the same prescribed element size, if the prescribed element sizes of their adjacent segments are different, the yielded element sizes for these two segments will be different. Block-2 is

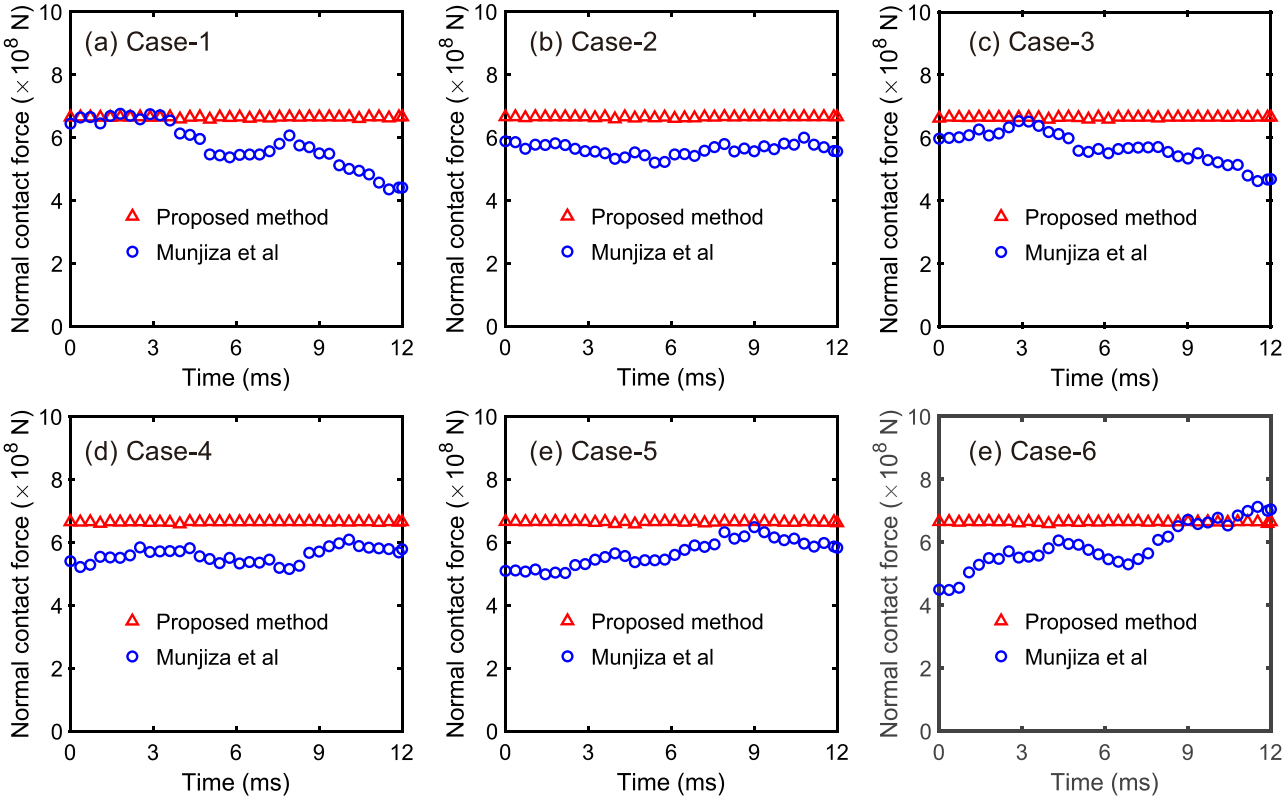

Fig. 8. Evolutions of normal contact force with time for both Munjiza's and the proposed method under different combinations of prescribed average element size for Block-2: (a) Case-1, (b) Case-2, (c) Case-3, (d) Case-4, (e) Case-5 and (f) Case–6.

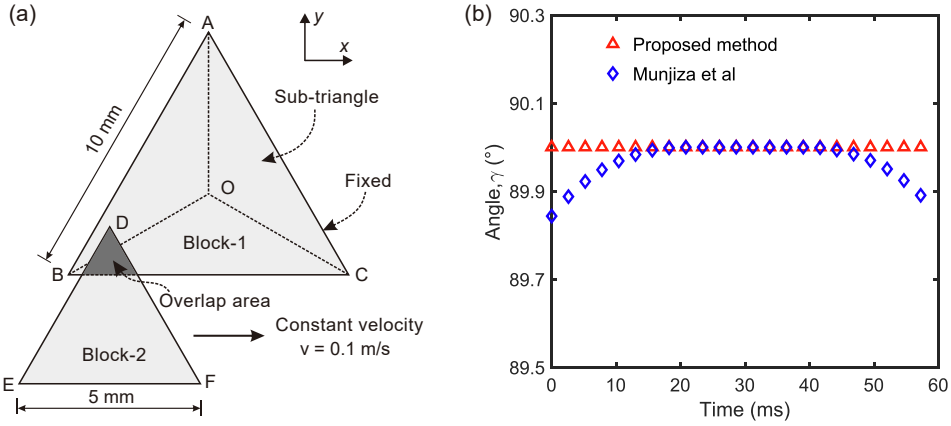

Fig. 9. (a) Model geometry. (b) Evolution of the normal contact force direction with time for Munjiza's and the proposed method.

fixed during the simulation, and a constant velocity of 5 m/s along the x axis is imposed on Block–1. The vertical direction of Block-1 is fixed, and thus a small amount of constant overlap area between Block-1 and Block–2 is maintained during the sliding process.

The parameters used for the model are as follows: Young's modulus $E = 30.0$ GPa, Poisson's ratio $\nu = 0.1$, bulk density $\rho = 2700$ kg/m^3, contact penalty $P_n = P_s = 300$ GPa, finite element viscous damping coefficient $\eta = 9.0 \times 10^4$ kg/m·s, and timestep $\Delta t = 6.0 \times 10^{-8}$ s. The gravity and the contact friction between the two blocks are not considered, and the total simulation time is 0.012 s. The unstructured Delaunay triangulation mesh scheme is utilized for Block-2, whereas Block-1 is discretized into four equal-size triangle elements (see Fig. 7b). The model consists of 279 triangle elements. As shown in Fig. 8, fluctuations of normal contact force during the sliding process are observed in Munjiza's method in all the six cases due to its dependence on element size for contact potential calculation. Fortunately, the normal contact forces calculated using the proposed approach in all cases remain nearly constant, which validates the robustness and correctness of the proposed approach in normal contact force calculation.

3.4. Normal contact force direction

Apart from the unstable contact force magnitude in the original FDEM demonstrated in Section 3.3, the definition of contact potential could also lead to non-smooth contact force direction when the contact point moves from one sub-triangle to another (Lei et al., 2020). This problem is also mentioned in previous works (Yan and Zheng, 2017; Zhao et al., 2018a,2018b). Here, two overlapped equilateral triangle finite elements (Block-1 and Block-2), with a side length of 10 mm and 5 mm, respectively, are designed to test the correctness of the proposed approach for contact force direction calculation. As shown in Fig. 9a, Block-1 is fixed, and a constant velocity of 0.1 m/s along the x axis is imposed on Block-2. The y direction of Block-2 is fixed, resulting in a constant overlap area between the two blocks during the sliding process. The parameters used for the model are as follows: Young's modulus $E = 30.0$ GPa, Poisson's ratio $\nu = 0.25$, bulk density $\rho = 2700$ kg/m^3, contact penalty $P_n = P_s = 300$ GPa, finite element viscous damping coefficient $\eta = 7.8 \times 10^4$ kg/m·s, and timestep $\Delta t = 2.6 \times 10^{-7}$ s. The gravity and contact friction between the two blocks are not considered, and the total simulation time is 5.72×10^{-2} s.

We denote the intersection angle between the calculated normal contact force direction and the x axis as γ (anticlockwise positive from the right). As shown in Fig. 9b, for Munjiza's approach, γ gradually increases when the location of contact transits from sub-triangle ΔABO to ΔBOC, and then γ gradually decreases when transiting from ΔBOC to ΔAOC. This indicates that when Block-2 is located near the two sides of sub-triangle ΔBOC, the calculated normal contact force direction using Munjiza's approach deviates from the correct direction, i.e., the y direction ($\gamma = 90°$). However, the normal contact force direction obtained by the proposed contact algorithm remains unchanged at $\gamma = 90°$ during the sliding process. This agrees with the physics that the geometric features between the two blocks are constant. Therefore, the proposed contact algorithm can effectively overcome the non-smooth transition of normal contact force direction.

3.5. Tangential contact force

To compare the tangential contact force calculated by Munjiza's

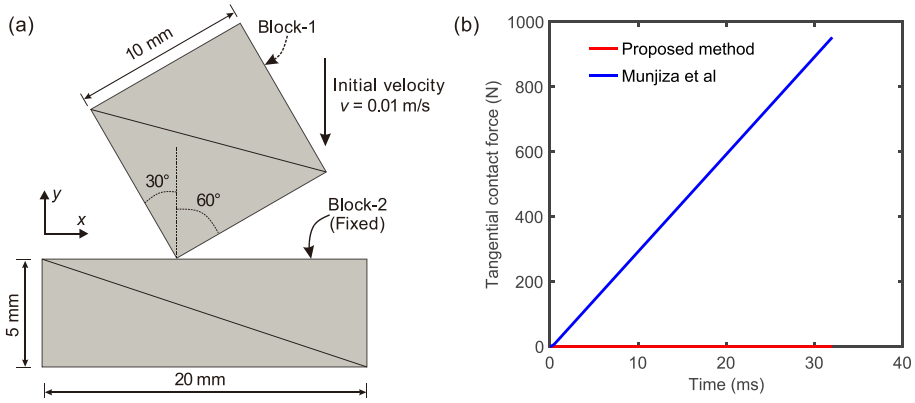

Fig. 10. (a) Geometric configuration of two blocks for tangential contact force calculation. (b) Evolution of tangential contact force with time for Munjiza's and the proposed method.

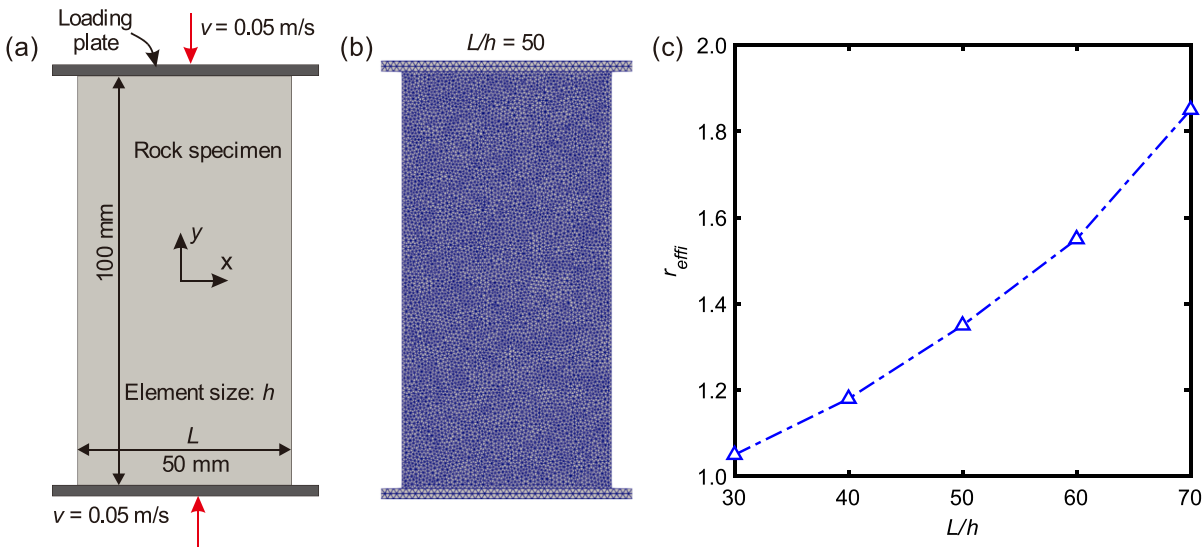

Fig. 11. (a) Model geometry and loading conditions. (b) Exemplar mesh with $L/h = 50$. (c) Comparison of the computational efficiency between the proposed method and Munjiza's method with various average element sizes. L denotes the width of the rock specimen; h is the average element size; r_{effi} is a ratio of the computing time needed between Munjiza's method and the proposed method upon reaching peak strength.

Table 2
Input parameters in FDEM simulations for UC tests.

Input parameters	Values
Young's modulus, E (GPa)	12.5
Bulk density, ρ (kg/m^3)	2400
Poisson's ratio, ν	0.25
Viscous damping coefficient, η (kg/m·s)	4300
Tensile strength, f_t (MPa)	2.0
Cohesion, c (MPa)	18
Internal friction angle, φ (°)	30
Mode I fracture energy, G_{f1} (J/m^2)	8
Mode II fracture energy, G_{f2} (J/m^2)	60
Normal contact penalty, P_n (GPa)	18
Tangential contact penalty, P_s (GPa)	62.5
Cohesive penalty, P_f (GPa)	125
Sample-plate friction coefficient, k_1 (-)	0.1
Sample friction coefficient, k_2 (-)	0.7

approach and the proposed approach, a contact test containing one square block (Block-1) and a rectangle block (Block-2) is performed (see Fig. 10a), where the edge length of Block-1 is 10 mm, and Block-2 has dimensions of 5 mm × 20 mm (height × width). Block-1, with a constant downward velocity of 0.01 m/s, is designed to penetrate the fixed Block-2 quasi-statically along the -y direction. No tangential displacement between the two blocks (along x direction) is allowed during the penetration. The parameters used for the model are as follows: Young's modulus $E = 30.0$ GPa, Poisson's ratio $\nu = 0.2$, bulk density $\rho = 2700$ kg/m^3, finite element viscous damping coefficient $\eta = 2.5 \times 10^5$ kg/m·s, contact penalty $P_n = P_s = 30$ GPa, friction coefficient $\mu = 0.2$, and timestep $\Delta t = 4.0 \times 10^{-7}$ s. Gravity is not considered. Each block is meshed into two triangle finite elements, and the total simulation time is $t = 0.032$ s. As shown in Fig. 10b, for Munjiza's approach, the tangential contact force gradually increases with time, which is inconsistent with the physics that no tangential contact force is supposed to occur between the two blocks due to the zero relative tangential displacement between them. Whereas for the proposed method, the tangential contact force remains unchanged at zero, validating the robustness of the proposed approach for tangential contact force calculation.

3.6. Computational efficiency

To further compare the computational efficiency between the proposed method and Munjiza's method, we perform a series of uniaxial compression (UC) tests. The model consists of two loading plates and a rock specimen, and the width and height of the rock specimen are 50 mm and 100 mm, respectively (see Fig. 11a). The axial loads are imposed on the specimens through the two loading plates moving inwards at a constant velocity of 0.05 m/s. Note that the loading rate can guarantee the quasi-static loading condition (Mahabadi et al., 2012; Tatone and Grasselli, 2015). The rock specimen is assumed to be homogeneous and isotropic, and the timestep is set as 1.5×10^{-8} s. We adopt the unstructured Delaunay triangulation mesh scheme to obtain reasonable fracture paths (see Fig. 11b). The input parameters for the FDEM simulations are tabulated in Table 2, which have been calibrated in previous work (Liu and Deng, 2019).

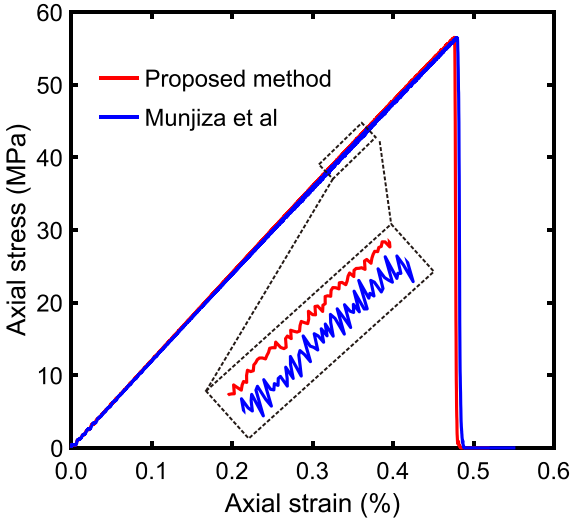

Fig. 12. Comparison of stress–strain response in terms of the proposed method and Munjiza's method.

For convivence, we define a variable r_{effi} to denote the ratio of the computing time needed between Munjiza's method and the proposed method, upon reaching the peak strength. The width of the rock specimen and average element size are denoted as L (50 mm) and h, respectively. We vary the element size h to form models with different

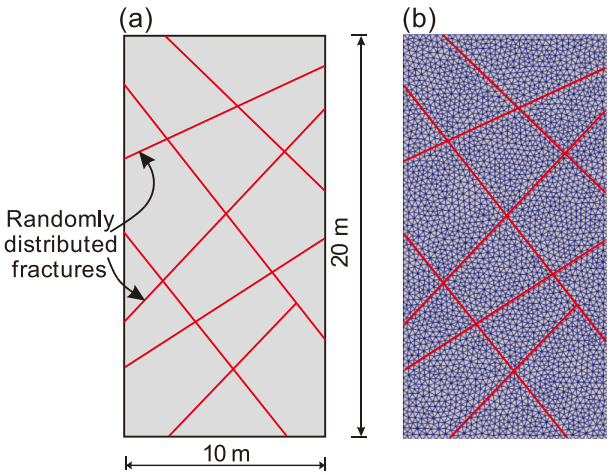

Fig. 13. (a) Model geometry of rock mass cut by randomly distributed fractures. (b) Mesh.

element numbers and record the corresponding computation time. As shown in Fig. 11c, with the increase of L/h, i.e., a decrease of element size and thus an increase in the number of finite elements, the efficiency index r_{effi} increases nonlinearly and reaches around 1.8 times when $L/h = 70$ (about 26,152 triangle elements). Therefore, the proposed method can slightly reduce computational cost compared to Munjiza's method. Furthermore, to further compare the mechanical response of the UC tests between the proposed method and Munjiza's method, we record the stress–strain curve obtained from the two methods. As shown in Fig. 12, the stress–strain curves of the two methods are generally consistent; however, more obvious stress fluctuations are encountered in Munjiza's method, indicating the robustness of contact calculation associated with UC tests simulated by the proposed method.

4. Application examples

In this section, two application examples are conducted to demonstrate the rationality of the proposed approach in simulating the stability of rock mass and rock slope. Since we mainly focus on testing the contact interaction between discrete bodies, fracturing rock blocks and joint cohesion are not considered in these cases.

4.1. Failure of rock mass

To demonstrate the failure mechanism of multiple block rock mass systems under gravity, we construct a rock mass model with dimensions of 10 m × 20 m (width × height). As shown in Fig. 13, randomly distributed fractures are adopted to cut the rock into arbitrarily shaped blocks. Different friction coefficients (i.e., μ = 0, 0.1, 0.2 and 0.3) between rock blocks are used, and no cohesion between rock blocks is considered. The bottoms of the rock model are in direct contact with the ground (not shown here). The parameters used are as follows: Young's modulus E = 30.0 GPa, Poisson's ratio $\nu = 0.27$, bulk density $\rho = 2700$ kg/m^3, gravitational acceleration g = -9.8 m/s^2, contact penalty $P_n = P_s = 90$ GPa, finite element viscous damping coefficient $\eta = 2.1 \times 10^6$ kg/m·s, timestep $\Delta t = 7.0 \times 10^{-6}$ s, and the total simulation time is 2.1 s. The model consists of 5833 triangle elements with an average size of 0.3 m, and the unstructured Delaunay triangulation mesh scheme is adopted (see Fig. 13b).

The collapse processes of the model with different block-block friction coefficients at various timestamps are presented in Fig. 14. It can be observed that the overall velocity of the rock masses gradually decreases with the increase of block-block friction coefficient, and only the upper rock blocks move when the friction coefficient is larger than 0.2. As the model evolves, the rock blocks are dumped laterally, and the velocities of the upper rock blocks are relatively larger than those at the bottom. The kinetic energy evolutions versus time are presented in Fig. 15. As the block-block friction coefficient increases from 0 to 0.4, the kinetic energy of the model gradually decreases. In addition, the kinetic energy of the models with zero block-block friction is obviously larger than others with nonzero friction coefficients, indicating that the contact friction can effectively dissipate the system's kinetic energy.

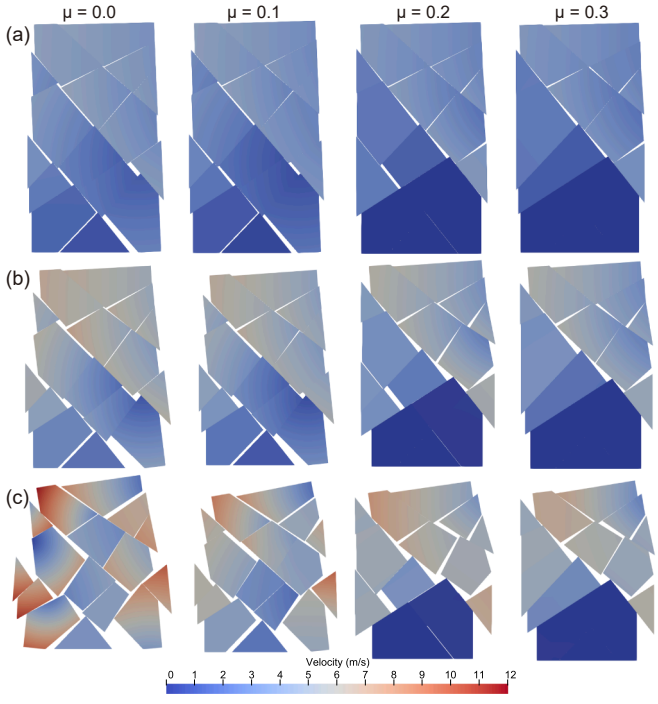

Fig. 14. The collapse process of the rock mass model with different block-block friction coefficients at various timestamps: (a) 0.42 s, (b) 0.63 s and (c) 0.84 s.

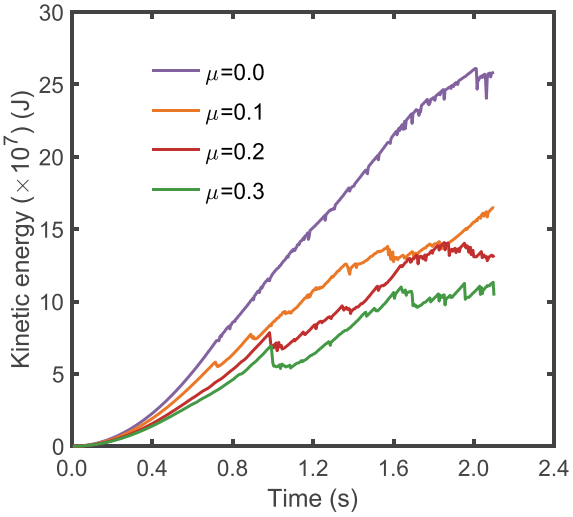

Fig. 15. Kinetic energy evolution versus time for the models with different block-block friction coefficients (μ = 0, 0.1, 0.2 and 0.3).

4.2. Vaiont landslide

We chose the Vaiont landslide (Sitar et al., 1997) that occurred in northern Italy to further simulate the rock slope sliding process at the engineering scale. The profile of the Vaiont landslide before and after the slide is shown in Fig. 16a. It can be observed that the whole slope mainly consists of rocks and a sliding base, where the rocks will slip along the sliding surface under gravity, and the sliding base is completely fixed. The parameters used are as follows: Young's modulus E = 10 GPa, Poisson's ratio ν = 0.3, bulk density ρ = 2300 kg/m^3, gravitational acceleration g = -9.8 m/s^2, contact penalty $P_n = P_s$ = 100 GPa, and simulated timestep $\Delta t = 2.0 \times 10^{-4}$ s. The model consists of 8750 triangle elements with an average size of 4.2 m, and the unstructured Delaunay triangulation mesh scheme is adopted (Fig. 16b). In addition, three monitoring points (denoted as MP-1, MP-2 and MP-3 in Fig. 16b respectively) are selected to track the evolution of their velocities. Note that the rocks are meshed into discrete triangle elements without cohesion between them, and the friction coefficients between the rocks and between the rock and the sliding base are 0.15 and 0.20, respectively. The selection of friction coefficient and other input parameters refer to the previous works (Wei et al., 2019; Zheng et al., 2014). In addition, to be consistent with the previous works (Wei et al., 2019; Zheng et al., 2014), the effect of groundwater level on slope sliding is also not considered, and we mainly focus on the mechanical behavior of contact interaction during rock sliding.

The resultant velocities of the three monitoring points with time and the snapshots of the slope sliding process are shown respectively in Fig. 17 and Fig. 18. It can be observed that the resultant velocities of the three monitoring points manifest a similar trend (Fig. 17), indicating that the rock slope moves forward as a whole. At the initial stage (see Fig. 18a), the resistance force of the rock slope stacked along the sliding surface is insufficient to maintain its stability, and the rocks slide down gradually. This rock slope movement is consistent with the increasing resultant velocities at the three monitoring points. As the model continues to evolve (Fig. 18b-c), the rocks first accumulate in the valley; then, their forward movement is obstructed by the slope on the other side of the valley. Meanwhile, the resultant velocities at the three monitoring points gradually decrease with time. The duration of the landslide process is around 30 s, which is consistent with that in the previous works (Wei et al., 2019; Zheng et al., 2014). When the sliding of the rock slope stops (Fig. 18d), the deposit profile of the simulated results mainly coincides with the actual topography.

5. Conclusions

In this study, within the framework of FDEM, a 2D energy-conserving contact model is adapted and implemented to simulate the contact interaction process between triangle elements. The magnitude of contact force is determined by the geometrical features of the overlapped region between contact couples, and the direction of contact force is obtained based on the gradient of contact potential field. The technique can not only guarantee energy conservation for elastic impacts, but also avoid the non-smooth transition of magnitude and direction of contact forces induced by the variation of element geometry in the original FDEM.

A series of numerical experiments are conducted to validate the correctness of the proposed contact algorithm. The block collision tests are conducted and the accuracy of the proposed contact algorithm for momentum conservation is validated. The classic friction experiment also verifies the accuracy of normal and tangential contact force calculation in the proposed approach. Compared to the original FDEM, the

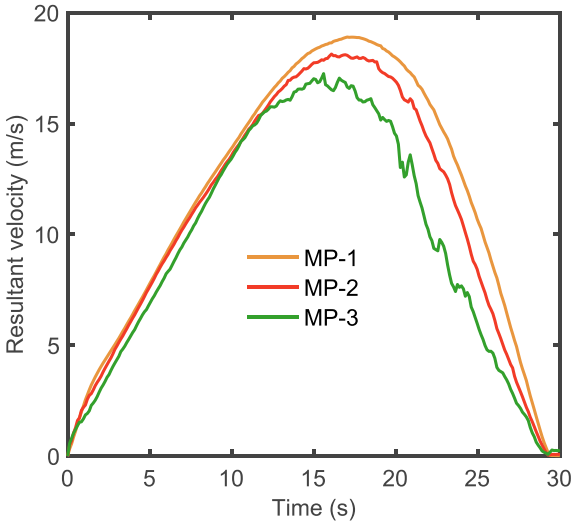

Fig. 17. The resultant velocity at the three monitoring points with time.

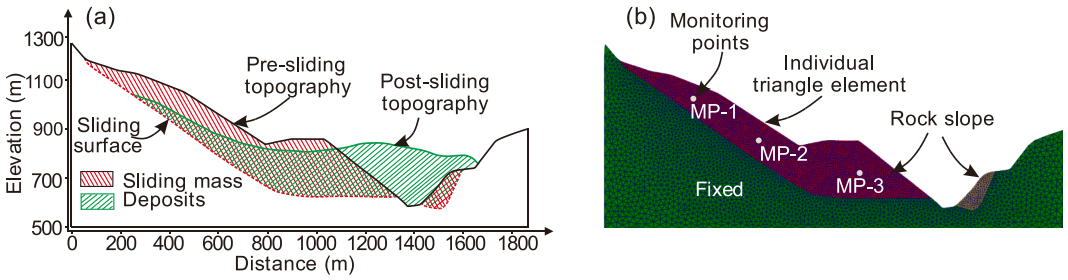

Fig. 16. (a) The typical cross-section of the Voiant landslide before and after sliding. (b) Mesh. Three monitoring points are denoted as MP-1, MP-2 and MP-3, respectively.

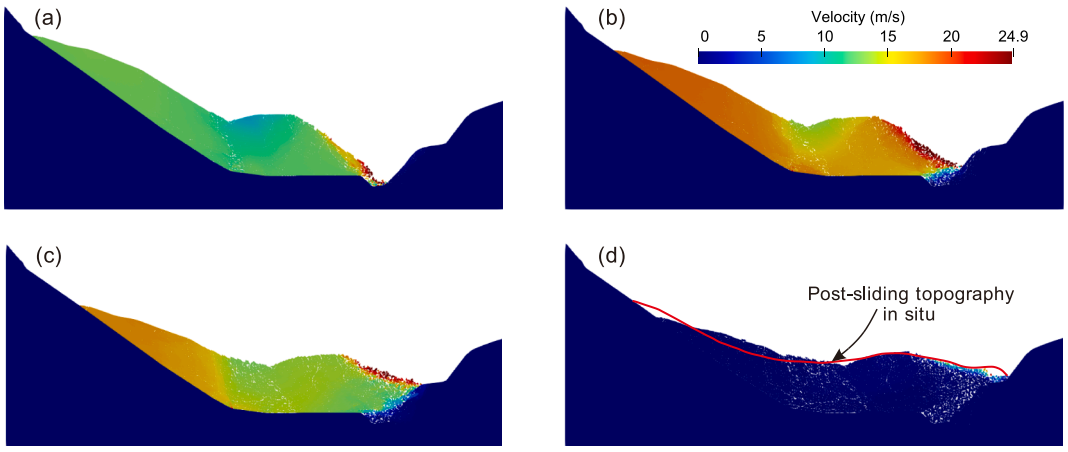

Fig. 18. Simulation results of the Vaiont landslide at different timestamps: (a) 9 s, (b) 15 s, (c) 21 s and (d) 30 s.

mesh size sensitivity tests prove that the normal contact force obtained from the proposed method is entirely mesh-independent. In addition, the proposed contact algorithm also avoids the non-smooth transition of normal contact force direction and the inaccurate evaluation of tangential contact force. Without considering the definition of contact point potential, the proposed method can slightly reduce the computational cost of contact interaction compared to Munjiza's method, and the stress–strain response of UC tests is more stable in the proposed method.

Following this, two application examples are conducted to demonstrate the rationality of the proposed approach for simulating rock mass and rock slope. The failure process of the rock mass model cut by randomly distributed fractures demonstrates that contact friction can effectively dissipate the system's kinetic energy. For the Vaiont landslide model at the engineering scale, the simulated deposit pattern of the Vaiont landslide is generally consistent with the actual topography. The proposed contact model can be readily implemented in the framework of FDEM, and it may help enhance the applicability and accuracy of FDEM for rock fracturing simulation. Extensions of the contact algorithm to 3D will be reported in the near future.

Declaration of Competing Interest

The authors declare that they have no known competing financial interests or personal relationships that could have appeared to influence the work reported in this paper.

Data availability

No data was used for the research described in the article.

Acknowledgments

This work is supported by the Shenzhen Science and Technology Program (JCYJ20220530113612028), the Guangdong Basic and Applied Basic Research Foundation (2023A1515011244), and the Guangdong Provincial Key Laboratory of Geophysical High-resolution Imaging Technology (2022B1212010002).

References

Board, M., 1989. UDEC (Universal Distinct Element Code) Version ICG1. 5. Nuclear Regulatory Commission, Washington, DC (USA). Div. of High-Level.
Chen, B., Xiang, J., Latham, J.-P., Bakker, R.R., 2020. Grain-scale failure mechanism of porous sandstone: An experimental and numerical FDEM study of the Brazilian Tensile Strength test using CT-Scan microstructure. Int. J. Rock Mech. Min. Sci. 132, 104348.
Cundall, P.A., Strack, O.D.L., 1979. A discrete numerical model for granular assemblies. Geotechnique. 29 (1), 47–65.
Deng, P., Liu, Q., Huang, X., Bo, Y., Liu, Q., Li, W., 2021a. Sensitivity analysis of fracture energies for the combined finite-discrete element method (FDEM). Eng. Fract. Mech. 251, 107793.
Deng, P., Liu, Q., Huang, X., Liu, Q., Ma, H., Li, W., 2021b. Acquisition of normal contact stiffness and its influence on rock crack propagation for the combined finite-discrete element method (FDEM). Eng. Fract. Mech. 242, 107459.
Euser, B., Rougier, E., Lei, Z., Knight, E.E., Frash, L.P., Carey, J.W., Viswanathan, H., Munjiza, A., 2019. Simulation of fracture coalescence in granite via the combined finite-discrete element method. Rock Mech. Rock Eng. 52 (9), 3213–3227.
Feng, Y., 2021a. A generic energy-conserving discrete element modeling strategy for concave particles represented by surface triangular meshes. Int. J. Numer. Methods Eng. 122 (10), 2581–2597.
Feng, Y.T., 2021b. An energy-conserving contact theory for discrete element modelling of arbitrarily shaped particles: Basic framework and general contact model. Comput. Meth. Appl. Mech. Eng. 373, 113454.
Feng, Y.T., 2021c. An energy-conserving contact theory for discrete element modelling of arbitrarily shaped particles: Contact volume based model and computational issues. Comput. Meth. Appl. Mech. Eng. 373, 113493.
Feng, Y.T., Han, K., Owen, D.R.J., 2012. Energy-conserving contact interaction models for arbitrarily shaped discrete elements. Comput. Meth. Appl. Mech. Eng. 205–208, 169–177.
Feng, Y.T., Owen, D.R.J., 2004. A 2D polygon/polygon contact model: algorithmic aspects. Eng. Comput. 21 (2), 265–277.
Gao, W., Feng, Y.T., 2019. A coupled 3D discrete elements/isogeometric method for particle/structure interaction problems. Comput. Part. Mech. 7 (5), 869–880.
Gu, D.M., Huang, D., Zhang, W.G., Gao, X.C., Yang, C., 2020. A 2D DEM-based approach for modeling water-induced degradation of carbonate rock. Int. J. Rock Mech. Min. Sci. 126, 104188.
Guo, L., Latham, J.-P., Xiang, J., 2015. Numerical simulation of breakages of concrete armour units using a three-dimensional fracture model in the context of the combined finite-discrete element method. Comput. Struct. 146, 117–142.
Han, H., Fukuda, D., Liu, H., Fathi Salmi, E., Sellers, E., Liu, T., Chan, A., 2020a. FDEM simulation of rock damage evolution induced by contour blasting in the bench of tunnel at deep depth. Tunn. Undergr. Space Technol. 103, 103495.
Han, H., Fukuda, D., Liu, H., Salmi, E.F., Sellers, E., Liu, T., Chan, A., 2020b. Combined finite-discrete element modelling of rock fracture and fragmentation induced by contour blasting during tunnelling with high horizontal in-situ stress. Int. J. Rock Mech. Min. Sci. 127, 104214.
Ju, Y., Liu, P., Chen, J., Yang, Y., Ranjith, P.G., 2016. CDEM-based analysis of the 3D initiation and propagation of hydrofracturing cracks in heterogeneous glutenites. J. Nat. Gas Sci. Eng. 35, 614–623.
Lai, Z., Zhao, S., Zhao, J., Huang, L., 2022. Signed distance field framework for unified DEM modeling of granular media with arbitrary particle shapes. Comput. Mech. 70 (4), 763–783.
Lei, Q., Gao, K., 2018. Correlation between fracture network properties and stress variability in geological media. Geophys. Res. Lett. 45 (9), 3994–4006.
Lei, Q., Gholizadeh Doonechaly, N., Tsang, C.-F., 2021. Modelling fluid injection-induced fracture activation, damage growth, seismicity occurrence and connectivity change in naturally fractured rocks. Int. J. Rock Mech. Min. Sci. 138, 104598.
Lei, Z., Rougier, E., Euser, B., Munjiza, A., 2020. A smooth contact algorithm for the combined finite discrete element method. Comput. Part. Mech. 7 (5), 807–821.
Lisjak, A., Liu, Q., Zhao, Q., Mahabadi, O.K., Grasselli, G., 2013. Numerical simulation of acoustic emission in brittle rocks by two-dimensional finite-discrete element analysis. Geophys. J. Int. 195 (1), 423–443.
Liu, Q., Deng, P., 2019. A numerical investigation of element size and loading/unloading rate for intact rock in laboratory-scale and field-scale based on the combined finite-discrete element method. Eng. Fract. Mech. 211, 442–462.
Liu, H., Ma, H., Liu, Q., Tang, X., Fish, J., 2022b. An efficient and robust GPGPU-parallelized contact algorithm for the combined finite-discrete element method. Comput. Meth. Appl. Mech. Eng. 395, 114981.

Liu, X., Mao, J., Zhao, L., Shao, L., Li, T., 2020. The distance potential function-based finite-discrete element method. Comput. Mech. 66 (6), 1477–1495.
Liu, G.-Y., Xu, W.-J., Zhou, Q., 2022a. DEM contact model for spherical and polyhedral particles based on energy conservation. Comput. Geotech. 153, 105072.
Mahabadi, O.K., Lisjak, A., Munjiza, A., Grasselli, G., 2012. Y-geo: new combined finite-discrete element numerical code for geomechanical applications. Int. J. Geomech. 12 (6), 676–688.
Munjiza, A., 1992. Discrete elements in transient dynamics of fractured media. Swansea University.
Munjiza, A., 2004. The combined finite-discrete element method. John Wiley, London.
Munjiza, A., Andrews, K.R.F., 1998. NBS contact detection algorithm for bodies of similar size. Int. J. Numer. Methods Eng. 43 (1), 131–149.
Munjiza, A., Knight, E.E., Rougier, E., 2011. Computational Mechanics of Discontinua. Willey, London.
Potyondy, D.O., Cundall, P.A., 2004. A bonded-particle model for rock. Int. J. Rock Mech. Min. Sci. 41 (8), 1329–1364.
Shi, G.H., Goodman, R.E., 1985. Two dimensional discontinuous deformation analysis. Int. J. Numer. Anal. Methods Geomech. 9 (6), 541–556.
Sitar, N., Maclaughlin, M., Tech, M., 1997. Kinematics and Discontinuous Deformation Analysis of Landslide Movement. In: Panamerican Symposium on Landslides.
Tatone, B.S.A., Grasselli, G., 2015. A calibration procedure for two-dimensional laboratory-scale hybrid finite–discrete element simulations. Int. J. Rock Mech. Min. Sci. 75, 56–72.
Wang, B., Li, H., Shao, Z., Chen, S., Li, X., 2021. Investigating the mechanism of rock fracturing induced by high-pressure gas blasting with a hybrid continuum-discontinuum method. Comput. Geotech. 140, 104445.
Wei, W., Zhao, Q., Jiang, Q., Grasselli, G., 2019. A new contact formulation for large frictional sliding and its implement in the explicit numerical manifold method. Rock Mech. Rock Eng. 53 (1), 435–451.
Wu, D., Li, H., Shao, Z., Chen, S., Zhou, C., Liu, L., 2021. Effects of infilling materials on mechanical behaviors and cracking process of pre-cracked rock: Insights from a hybrid continuum-discontinuum method. Eng. Fract. Mech. 253, 107843.
Xiang, J., Chen, B., Latham, J.-P., Pain, C., 2022. Numerical simulation of rock erosion performance of a high-speed water jet using an immersed-body method. Int. J. Rock Mech. Min. Sci. 158, 105179.
Yan, C., Jiao, Y.-Y., Yang, S., 2018. A 2D coupled hydro-thermal model for the combined finite-discrete element method. Acta Geotech. 14 (2), 403–416.
Yan, C., Xie, X., Ren, Y., Ke, W., Wang, G., 2022. A FDEM-based 2D coupled thermal-hydro-mechanical model for multiphysical simulation of rock fracturing. Int. J. Rock Mech. Min. Sci. 149, 104964.
Yan, C.Z., Zheng, H., 2017. A new potential function for the calculation of contact forces in the combined finite-discrete element method. Int. J. Numer. Anal. Methods Geomech. 41 (2), 265–283.
Yang, P., Lei, Q., Xiang, J., Latham, J.-P., Pain, C., 2020. Numerical simulation of blasting in confined fractured rocks using an immersed-body fluid-solid interaction model. Tunn. Undergr. Space Technol. 98, 103352.
Zhao, Q., Lisjak, A., Mahabadi, O., Liu, Q., Grasselli, G., 2014. Numerical simulation of hydraulic fracturing and associated microseismicity using finite-discrete element method. J. Rock Mech. Geotech. Eng. 6 (6), 574–581.
Zhao, L., Liu, X., Mao, J., Xu, D., Munjiza, A., Avital, E., 2018a. A novel contact algorithm based on a distance potential function for the 3D discrete-element method. Rock Mech. Rock Eng. 51 (12), 3737–3769.
Zhao, L., Liu, X., Mao, J., Xu, D., Munjiza, A., Avital, E., 2018b. A novel discrete element method based on the distance potential for arbitrary 2D convex elements. Int. J. Numer. Methods Eng. 115 (2), 238–267.
Zhao, Q., Tisato, N., Grasselli, G., Mahabadi, O.K., Lisjak, A., Liu, Q., 2015. Influence ofin situstress variations on acoustic emissions: a numerical study. Geophys. J. Int. 203 (2), 1246–1252.
Zheng, W., Zhuang, X., Tannant, D.D., Cai, Y., Nunoo, S., 2014. Unified continuum/discontinuum modeling framework for slope stability assessment. Eng. Geol. 179, 90–101.